



HAL
open science

Reconfigurable flexural waves manipulation by broadband elastic metasurface

Si-Min Yuan, A-Li Chen, Xing-Yue Du, Hua-Wei Zhang, Badreddine Assouar,
Yue-Sheng Wang

► **To cite this version:**

Si-Min Yuan, A-Li Chen, Xing-Yue Du, Hua-Wei Zhang, Badreddine Assouar, et al.. Reconfigurable flexural waves manipulation by broadband elastic metasurface. *Mechanical Systems and Signal Processing*, 2022, 179, pp.109371. 10.1016/j.ymssp.2022.109371 . hal-03843393

HAL Id: hal-03843393

<https://hal.science/hal-03843393>

Submitted on 8 Nov 2022

HAL is a multi-disciplinary open access archive for the deposit and dissemination of scientific research documents, whether they are published or not. The documents may come from teaching and research institutions in France or abroad, or from public or private research centers.

L'archive ouverte pluridisciplinaire **HAL**, est destinée au dépôt et à la diffusion de documents scientifiques de niveau recherche, publiés ou non, émanant des établissements d'enseignement et de recherche français ou étrangers, des laboratoires publics ou privés.

Reconfigurable Flexural Waves Manipulation by Broadband Elastic Metasurface

Si-Min Yuan^a, A-Li Chen^{a,*}, Xing-Yue Du^a, Hua-Wei Zhang^a, Badreddine Assouar^{c,*}, Yue-Sheng Wang^{a,b*}

^a Institute of Engineering Mechanics, Beijing Jiaotong University, Beijing 100044, China

^b Department of Mechanics, Tianjin University, Tianjin, 300350, China

^c Université de Lorraine, CNRS, Institut Jean Lamour, Nancy 54000, France

* Corresponding authors: alchen@bjtu.edu.cn (AL Chen) ; badreddine.assouar@univ-lorraine.fr (B Assouar); yswang@bjtu.edu.cn, yswang@tju.edu.cn (YS Wang)

Abstract

We propose a reconfigurable elastic metasurface for broadband plate wave control where the flexural-dominated plate mode is concerned. The structure consists of a plate with nuts and screws perpendicular to the plate. With the continuous changes of nut positions on the screws, the phase shift can cover 2π span with high transmittance over broadband frequency. The mechanism of the tunability of phase shift caused by the screw-in depth is discussed based on the dispersion theory of local resonant phononic crystals. Then, subwavelength elastic metasurfaces are designed based on the generalized Snell's law demonstrating numerically and experimentally abnormal refraction and wave focusing functionalities without remanufacturing the metasurface. Furthermore, we show asymmetric transmission with a structure containing two parallel metasurfaces. Different functionalities can be achieved by changing the screw-in depth at different frequencies. The proposed metasurface designs could provide a novel and feasible route to control flexural waves in broadband frequency range and take a critical step in the pragmatic development of elastic metasurfaces.

Keywords: Elastic metasurfaces; Flexural waves; Reconfigurability; Broadband; Phase modulation; Wavefront control.

Introduction

Metamaterials can give unique characteristics that cannot exist in conventional materials [1]. However, further applications of metamaterials have been restricted because of their bulky and heavy characteristics [2]. Metasurfaces, which can be considered as a two-dimensional (2D) counterpart of metamaterials, have opened up possibilities for realizing extraordinary wave manipulation with lightweight and thin planar designs [3-5]. After optic [6, 7] and acoustic metasurfaces [8-12], elastic metasurfaces have been gradually developed because of their excellent manipulation ability of elastic waves.

Most studies on elastic metasurfaces focus on the plate waves, and so does this paper. The phase shift of elastic waves can be tuned mainly by changing their velocities through a resonant or non-resonant way. Usually, the former can be achieved by

introducing resonant units such as pillars or columns [13-20], zigzag units [21-25], and blocks [26-30] into the structure. The latter, however, can be realized by grooves [31], notched units [32], strips [33, 34] or composite strips [35, 36], etc. Full phase control can also be achieved by gradient-index phononic crystals [2]. However, the dimension of the structure is much larger than the wavelength. According to the abovementioned methods, researchers have proposed various metasurfaces to steer the wavefronts of refracted plate waves. Anomalous refraction of Lamb wave [13] was first realized by a metasurface composed of tapered resonance units. By erecting pillars or columns perpendicularly on a plate, metasurfaces were designed with changing the heights of the pillars or columns to manipulate flexural waves [14-19]. Cao et al. [20] also discussed the identical pillared resonators with a random arrangement. In-plate [21-24] and out-of-plate [25] zigzag units were proposed to design metasurfaces for source illusion, refraction, focus, asymmetric transmission and ultrathin waveguide of A0 Lamb waves. Changing the sizes of resonant blocks added to beams was also able to manipulate the phase of the transmitted flexural wave [26]. Making slits or openings on a plate can form resonant units for the deflection of longitudinal wave [27] and broad-angle modal conversion between P- and SV-waves [28] in plates. With the similar structure of Ref. [28], a double-unit elastic metasurface composed of a phase modulator and an impedance matcher was proposed to realize full-wave tailoring of longitudinal wave [29]. Topology optimization was utilized to obtain resonant units for the deflection and focus of a plate longitudinal wave [30].

As for the non-resonant way, the phase manipulation and different functions of S0 Lamb wave were realized by changing the groove positions in the groove array structure [31]. A notched metasurface provides an innovative way to manipulate flexural waves without resonators, which supports high transmittance and multi-parameter modulation [32]. Various functionalities of in-plane waves [33] and S0 waves [34] in plates were achieved via designing the thickness of the straight beam unit. The straight beam can be replaced by a composite beam or strip consisting of two different materials [35, 36].

However, the aforementioned metasurfaces can only work for a certain function at a fixed frequency or an extremely narrow frequency range, which limits their practical applications [37]. To break these restrictions, tunable metasurfaces have been proposed with the help of piezoelectric materials or mechanical reconfigurability of the structure. In fact, piezoelectric units with feedback circuits have been widely applied in smart wave control in phononic crystals and metamaterials, cf. Ref. [38] among others. In Ref. [39], piezoelectric resonant units were proposed to design a tunable metasurface which can realize directional refraction, wave focusing and source illusion of A0 Lamb wave by adjusting the negative capacitance. The similar method was used to design a tunable metasurface for SH0 wave modulation [40]. And the real time control of a broadband flexural wave was achieved via a programmable metasurface based on the piezoelectric unit and feedback circuit control [41]. Recently, we proposed a fish-bone mechanically reconfigurable elastic metasurface to manipulate the wave front of flexural [42] and in-plane waves [43] based on the “screw-and-nut” working principle. By changing the positions of the nuts on the screws, the phase shift of the transmitted wave can be manipulated continuously with high transmittance. Mechanical reconfiguring methods

were usually used in design linear or nonlinear meta-structured materials [44].

Recent researches on the structure-based reconfigurable elastic metasurfaces without a complex system are relatively scarce. In this paper, the “screw-nut” structure is improved to make the metasurface easy to fabricate; and then different functionalities for the refracted flexural-dominated wave are demonstrated numerically and experimentally. The proposed broadband elastic metasurface could make a significant progress in the practical applications.

Element design and phase shift analysis

Unlike the previous fish-bone model for which the screws are paralleled to the plate [42, 43], in this paper we improve the structure by making the screws perpendicular to the plate which will be more efficient for steering the flexure wave and can facilitate the fabrication of metasurfaces. The calculation models of basic unit and functional element are shown in Figs. 1(a) and (b). The gray and green regions represent the substrate (aluminum) and vibrators (steel), respectively. The material parameters of aluminum are as follows: mass density $\rho = 2700 \text{ kg/m}^3$, elastic modulus $E = 68.9 \text{ GPa}$ and Poisson's ratio $\nu = 0.33$, and those of steel are $\rho = 7670 \text{ kg/m}^3$, $E = 199.4 \text{ GPa}$ and $\nu = 0.31$. The influences of the geometric parameters shown in Fig. 1(a) on the modulation of phase shift and transmittance are discussed in Appendix A. Base on the results therein, we select a model of the functional element with 6 basic units in the following analysis and take the values of other geometric parameters as shown in Table 1. The screw-in depth (s) refers to the distance that the nut moves inward from the outer end of the column, as shown in Fig. 1(a). Notably, the distance between the front and back rows of the nuts and the plate is always keeping the same. Fig. 1(c) is the photograph of a functional element corresponding to Fig. 1(b).

For harmonic waves propagating in the inhomogeneous isotropic solids, the wave equation can be written as the following form by omitting the time harmonic term:

$$\nabla \left[(\lambda(\mathbf{r}) + 2\mu(\mathbf{r})) (\nabla \cdot \mathbf{u}) \right] - \nabla \times [\mu(\mathbf{r}) \nabla \times \mathbf{u}] = -\rho(\mathbf{r}) \omega^2 \mathbf{u}, \quad (1)$$

where $\nabla = (\partial/\partial x, \partial/\partial y, \partial/\partial z)$ is the differential operator; λ and μ are the Lamé

constants; $\mathbf{r} = (x, y, z)$ is the position vector; $\mathbf{u} = (u_x, u_y, u_z)$ is the displacement vector and $\omega = 2\pi f$ is the circular frequency. In this paper, the finite element method is used to study the wave properties. A line source with the out-of-plane excitation is applied on the left side of the functional element. The phase shift and transmittance can be obtained by taking the averaged values along the detection line of the right side. Continuous periodic conditions are applied on the upper and lower boundaries, i.e.

$$\mathbf{u}_u = \mathbf{u}_d, \quad (2)$$

where \mathbf{u}_u and \mathbf{u}_d are the displacements of the upper and lower surfaces, respectively. In order to attenuate reflection, perfectly matched layers (PMLs) are set on the left and right ends. The phase shift of the transmitted wave is regulated by changing the screw-in depth (s) of the nuts.

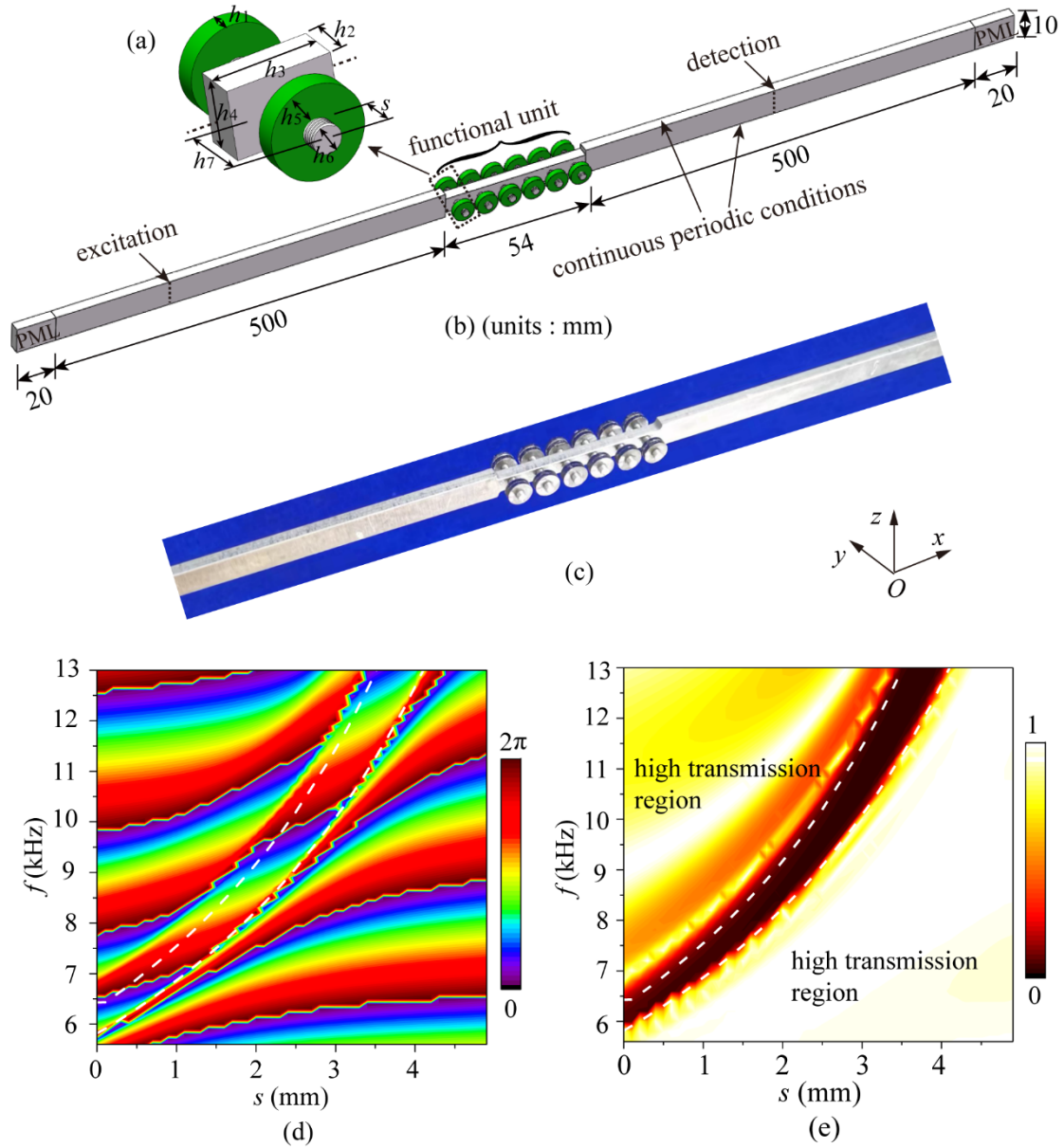


Fig. 1 The basic unit (a) and the strip model with functional element (b) in numerical calculations; (c) the photograph of the strip specimen; the calculated nephograms of the phase shift (d) and transmittance (e) as functions of the screw-in depth s and frequency.

The phase shift and transmittance are calculated by the finite element method with the software COMSOL Multiphysics 5.4; and their variations with the frequency and screw-in depth are illustrated in the nephograms shown in Figs. 1(d) and (e). It is noted that the step of screw-in depth is 0.01mm which can be realized by rotate the nut by a certain angle (α). The relation between s and α is $s = t \times \alpha / 360$ where t is the thread pitch. In the present design, we choose $t = 0.5$ mm. Thus the precision of 0.01mm for the screw-in depth corresponds to $\alpha = 7.2^\circ$ which can also be easily realized in the experiments. The results shown in Fig. 1(d) demonstrate that the phase shift can cover a 2π period in broadband when s is changed continuously. It should be noticed that the appearance of “sudden changes” in the phase shift nephogram is due to the “phase fold”

at $\phi = 2m\pi$ when the phase shift exceeds $2m\pi$ ($m = 1, 2, 3 \dots$) [42, 43].

The transmittance ξ_f is calculated by

$$\xi_f = \frac{A_1}{A_0}, \quad (3)$$

where A_1 is the transmitted out-of-plane displacement amplitude of the strip model with a functional element shown in Fig. 1(b); and A_0 is that for the uniform structure without the ‘‘screw-nuts’’. The transmittance within the two white dotted lines (the black zone in Fig. 1 (e)) is very low, so we should avoid this zone when designing the metasurface.

To interpret the mechanism of phase manipulation of the functional element shown in Fig. 1(b), we consider it as a finite structure intercepted from a one-dimensional locally resonant phononic crystal with the periodically distributed basic units (Fig. 1(a)) along x direction. Based on the Bloch’s theory, the wave field satisfies:

$$\mathbf{u}(x+a) = \mathbf{u}(x) \exp(-i k_x a), \quad (4)$$

where k_x is the Bloch wave vector; and a is the lattice constant (here it is 9 mm), as shown in Fig. 1(a)). Then, the dispersion curves of different screw-in depths are calculated; and the results for $s = 1.3, 2.9$ and 4.5 mm are shown in Fig. 2(a). The color of the bands represents the proportion of the out-of-plane displacement to the total displacement defined as

$$\eta = \frac{\left| \int_{V_p} u_y dV \right|}{\left| \int_{V_p} \sqrt{u_x^2 + u_y^2 + u_z^2} dV \right|}, \quad (5)$$

where the integrals are taken over the volume (V_p) of the rectangular plate of basic unit. $\eta \rightarrow 1$ (the dark red color) represents the flexure-dominated wave modes. The displacement modes of the basic unit are shown in the insets of Fig. 2(a). The flexural mode of the plate is mainly caused by the symmetric vibration mode ($k_x = 0.5\pi/a$) of the resonant structure (screw-nut), corresponding to the red part of band I. There are also a few antisymmetric vibration modes ($k_x = \pi/a$), corresponding to the blue part of Band I.

Table 1. Geometric parameters (unit: mm).

h_1	h_2	h_3	h_4	h_5	h_6	h_7
3	4	9	6	2.5	3	8

By observing Band I dominated by out-of-plane displacement, it can be clearly seen that with the increase of s , the band is getting steeper indicating the increase of the phase velocity c_p . For a given frequency, the phase velocity can be calculated from the dispersion curve through $c_p = 2\pi f/k$ where k is the wave number. For example, c_p varying with s at $f = 6.4$ kHz can be calculated from the crosspoints of the dot-line and Band I; and the results are shown in Fig. 2(b). Then, when the wave propagates through the functional element, the phase shift ϕ can be calculated by

$$\phi = 2\pi fl/c_p, \quad (6)$$

where l is the length of the “screw-nut” structure i.e. the thickness of the metasurface (here it is 54 mm). The phase shifts (the blue dots) calculated from the phase velocity curve are close to the simulated ones (the black curve), as shown in Fig. 2(c).

By the way, the low transmittance region mentioned above can also be interpreted by the dispersion curves. As shown in Fig. 2(a), there is a band gap (gray region) between the two red passbands. Taking $s = 1.3$ mm as an example, the band gap for the flexural wave shown in Fig. 2(a) is (7.2 – 8.0 kHz) which is exactly the same region of the black zone shown in Fig. 1(e).

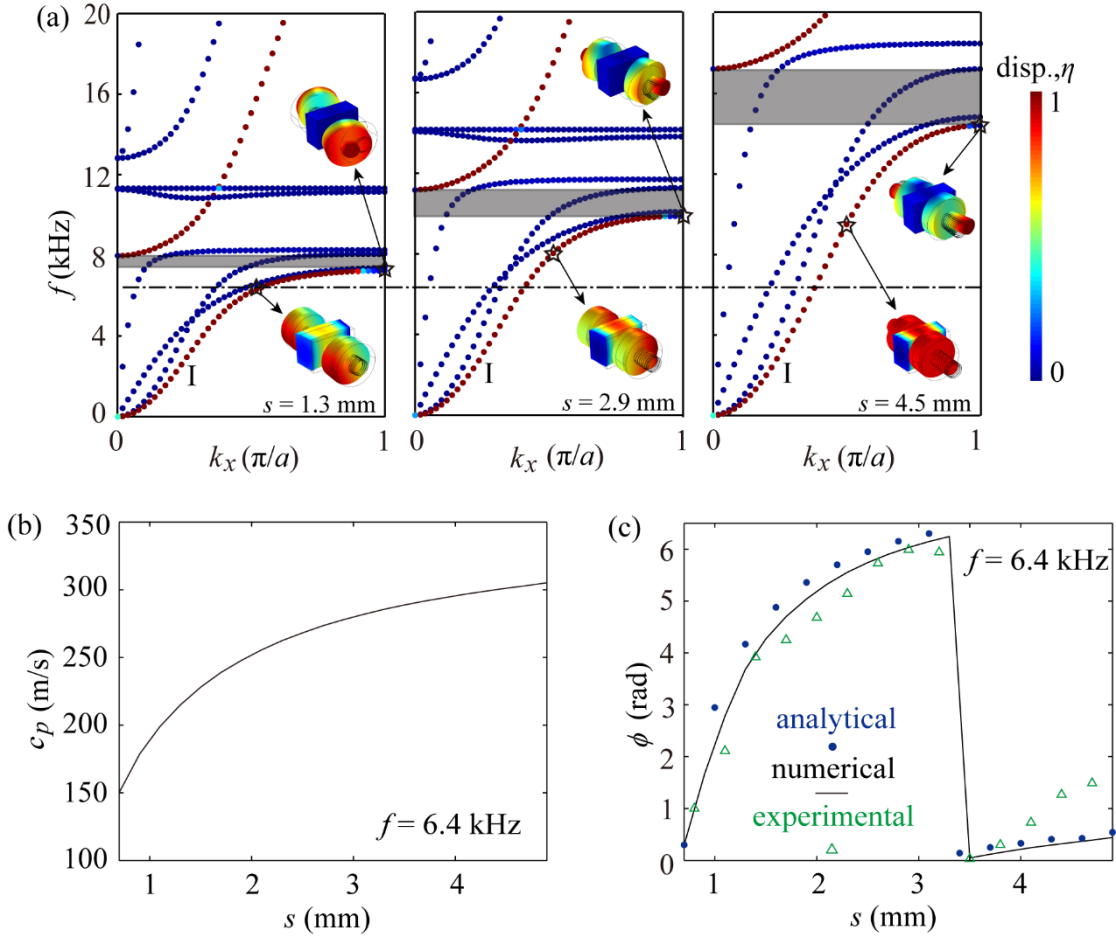


Fig. 2 (a) The dispersion curves and the displacement modes for the screw-in depth $s = 1.3, 2.9$ and 4.5 mm; (b) the phase velocity curve varying with s for $f = 6.4$ kHz; and (c) the phase shifts obtained by numerical simulation (the black curve), analytical calculation (the blue dots) and experiment (the green triangles) for $f = 6.4$ kHz.

The phase regulating capacity of the functional element is also examined experimentally in this paper. The experiment setups and the specimen (1054 mm \times 10 mm \times 4 mm) are shown in Figs. 3(a) and (b). The Polytec PSV-500 generated a sinusoidal signal of $f = 6.4$ kHz which was transmitted to the piezoelectric patch (10 mm \times 10 mm \times 1 mm) shown in Fig. 3(c) through the power amplifier (AG1020). The

phase values on the line (see Fig. 3(d)) in the transmitted field were picked up by the laser scanning vibrometer Polytec PSV-500. The big enough homogeneous regions with the blue-tacks glued on the upper and lower boundaries of the specimen [13, 14] can reduce the wave reflection well. Changing the screw-in depths of the nuts and repeating the above operations, we can get the phase shifts which are shown by the scattered green triangles in Fig. 2(c).



Fig. 3. (a) The experimental setup; (b) the functional element suspended on a vibration isolation table; the zoomed-in diagrams of (c) piezoelectric patch, and (d) measuring line of the phase shift; (e) the manufactured plate; and (f) the zoomed-in diagram of the metasurface structure and piezoelectric patches array.

The experimental results match well with the theoretical and numerical ones when $s \leq 4$ mm. The large difference for $s > 4$ mm may be owing to the fact that the sample is not strictly symmetrical due to processing errors. With the increase of s , the resonance of the basic unit (screw with a nut) gradually weakens, and other wave modes (e.g. the torsional modes) may be relatively enhanced, which affects the experimental results. Fortunately, it can be seen from Appendix B (Tables B1-B3) that most values of s are smaller than 4 mm. So this phenomenon has little impact on the ultimate goal of the present design of the metasurface to achieve different functionalities. Anyway, the sample processing and measurement deserve improvement in future studies.

Metasurfaces design and numerical simulations of multiple functionalities in broadband

In this section, we will design the metasurface based on the GSL [45] to realize the manipulation of transmitted flexural waves. First, abnormal refraction with arbitrary refracted angles and wave focusing with arbitrary focus positions are realized numerically in broadband by a single metasurface. Then, a double-layered metasurface system is constructed to achieve the asymmetric transmission under different operating frequencies.

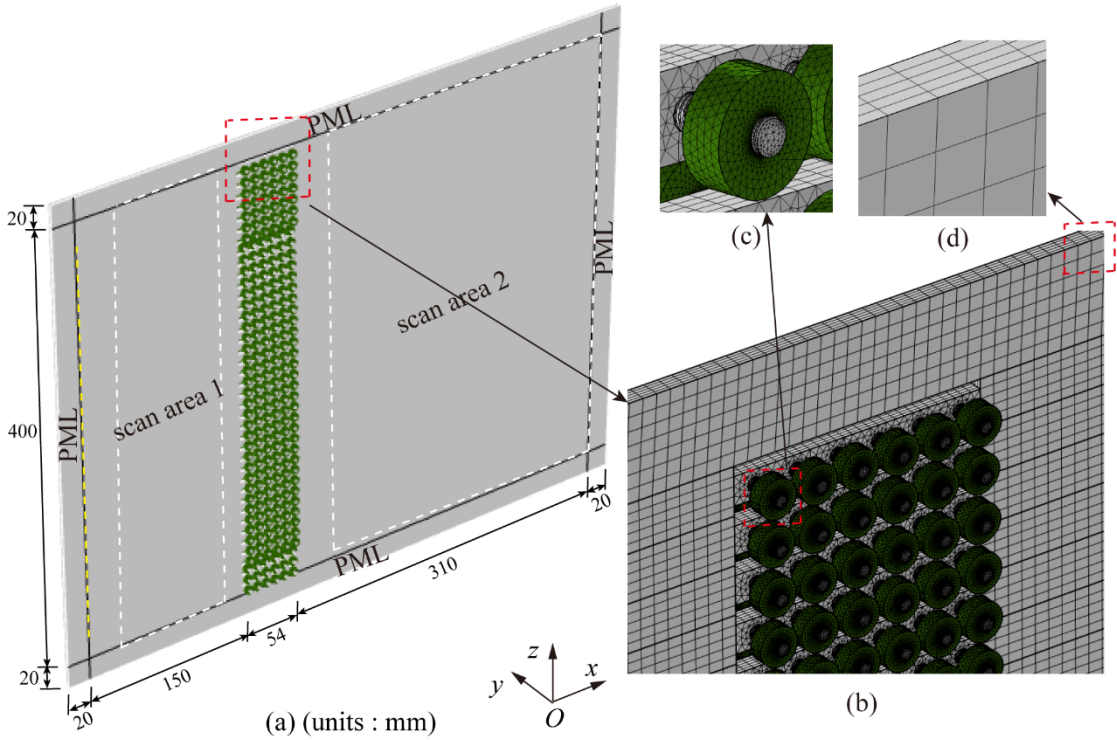


Fig. 4. The calculation model of the metasurface (a) and its finite element meshes (b) established in COMSOL Multiphysics. (c) and (d) are the partial enlargements of (b).

The calculation model of a single metasurface with 40 functional elements is shown in Fig. 4(a). The boundaries around the model are set as PMLs. An edge load along the y -direction with the amplitude of $1 \cdot \exp[-(z - \alpha H)^2 / w_0^2]$ (N/m) is applied at the

yellow dashed line to excite a Gaussian beam, where $H = 10$ mm is the height of the functional element, as shown in Fig. 1(b). Multi-functionalities such as directional refraction ($\alpha = 23.5$ and $w_0 = 0.1$), wave focusing ($\alpha = 0$ and $w_0 = 0.4$) and asymmetric transmission ($\alpha = 19.5$ and $w_0 = 0.1$) will be realized numerically.

The finite element meshes ensuring the convergence of calculation are shown in Figs. 4(b)-(d). Sparse meshes are first built for calculation, and then the mesh density gradually increases until the results no longer change, that is, the results are convergent. The strips which contain resonant units are meshed by triangular prism elements and divided into 5 layers in y -direction (Fig. 4(c)). The remaining parts of substrate are also divided into 5 layers in y -direction by cuboid elements (Fig. 4(d)). The screws and nuts are meshed by tetrahedral elements (Fig. 4(c)) with the extremely fine size, which predefined in COMSOL Multiphysics.

In this paper, for the transmitted wave propagating along the designated direction, the required phase distribution can be calculated from the following refracted GSL:

$$\sin \theta_t - \sin \theta_i = \frac{\lambda_0}{2\pi} \frac{d\phi(z)}{dz}, \quad (7)$$

where θ_t and θ_i are refraction and incident angles, respectively; $\phi(z)$ is the phase distribution along the metasurface which should be discretized during the design of the metasurface; and $\lambda_0 = c/f$ is the wavelength with c being the phase velocity of the flexural wave [33]:

$$c = \sqrt[4]{\frac{E_1 h_2^2 \omega^2}{12 \rho_1 (1 - \nu_1^2)}}, \quad (8)$$

where h_2 is the thickness of the plate (here it is 4 mm). Once the phase shifts are known, we can obtain the corresponding screw-in depth of each functional element according to Fig. 1(d). Then the metasurface with the function of abnormal refraction can be constructed. For different refracted angles or operating frequencies, the metasurfaces can be reconfigured just by tuning the positions of the nuts.

The screw-in depths of the n th functional element ($n = 1-40$) for different refraction angles in case of $f = 6.4, 8.6$ and 11.2 kHz (the corresponding wavelengths are 77.9, 67.2 and 58.9 mm, respectively) are listed in Tables B1 ($\theta_t = 15^\circ, 50^\circ$) and B3 ($\theta_t = 90^\circ$) in Appendix B. The results are shown in Fig. 5 in which the out-of-plane displacement fields are presented. It can be seen that for different operating frequencies, the transmitted waves can propagate along the designated directions ($\theta_t = 15^\circ, 50^\circ$ and 90°) as marked by the arrows in Fig. 5. In conclusion, the designed tunable metasurface can realize the directional refraction of an arbitrary refracted angle under different frequencies. Besides, we notice that some undesired beams appear in addition to the designed angles, especially for the cases of 50° - and 90° -refractions. These unwanted beams stem from the high-order diffractions which become pronounced in the case of large angle refraction [46, 47].

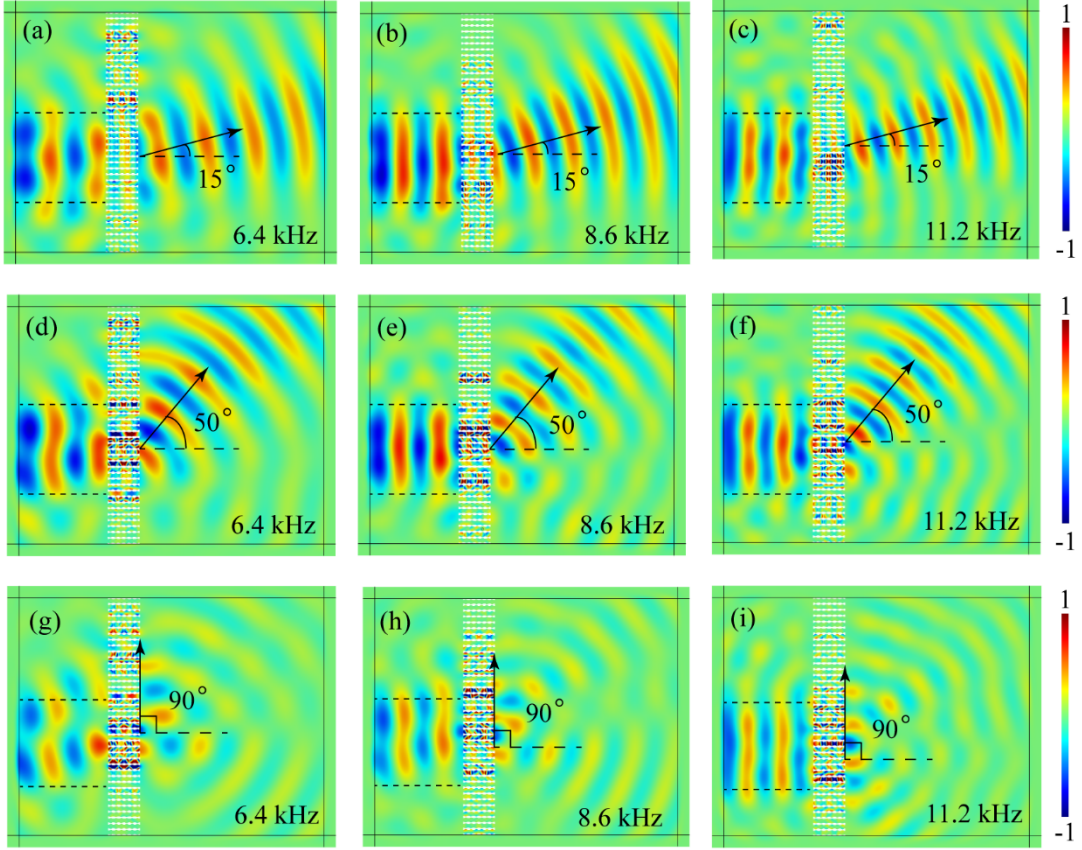


Fig. 5. The out-of-plane displacement fields for $f=6.4, 8.6$ and 11.2 kHz. The refraction angles are (a)-(c) 15° , (d)-(f) 50° and (g)-(i) 90° .

Next, the wave focusing is demonstrated by adjusting the screw-in depths of the nuts of the designed metasurface. Given the desired focal positions (x, z) , the required phase shifts are thereupon determined by [42, 43]

$$\phi_n - \phi_1 = \frac{2\pi}{\lambda_0} (\sqrt{(z_n - z)^2 + x^2} - \sqrt{(z_1 - z)^2 + x^2}), n = 2, 3, 4 \dots \quad (9)$$

where ϕ_1 and ϕ_n are the phase shifts of the first and n th ($n > 1$) functional elements of the metasurface, respectively; z_1 and z_n are the z coordinates of the first and n th functional elements of the metasurface, respectively. Likewise, by combining Fig. 1(d), the screw-in depth for each functional element of the metasurface can be obtained. The corresponding screw-in depths of different focal positions $(x, z) = (150 \text{ mm}, 0)$ and $(200 \text{ mm}, 0)$ in case of $f = 6.4, 8.6$ and 11.2 kHz can be found in Table B2 in Appendix B. Fig. 6 shows the intensity of the out-of-plane wave fields. The positions of the focal points are basically matched with the default positions $(150 \text{ mm}, 0)$ and $(200 \text{ mm}, 0)$. All results show good focus capability of the proposed reconfigurable elastic metasurface.

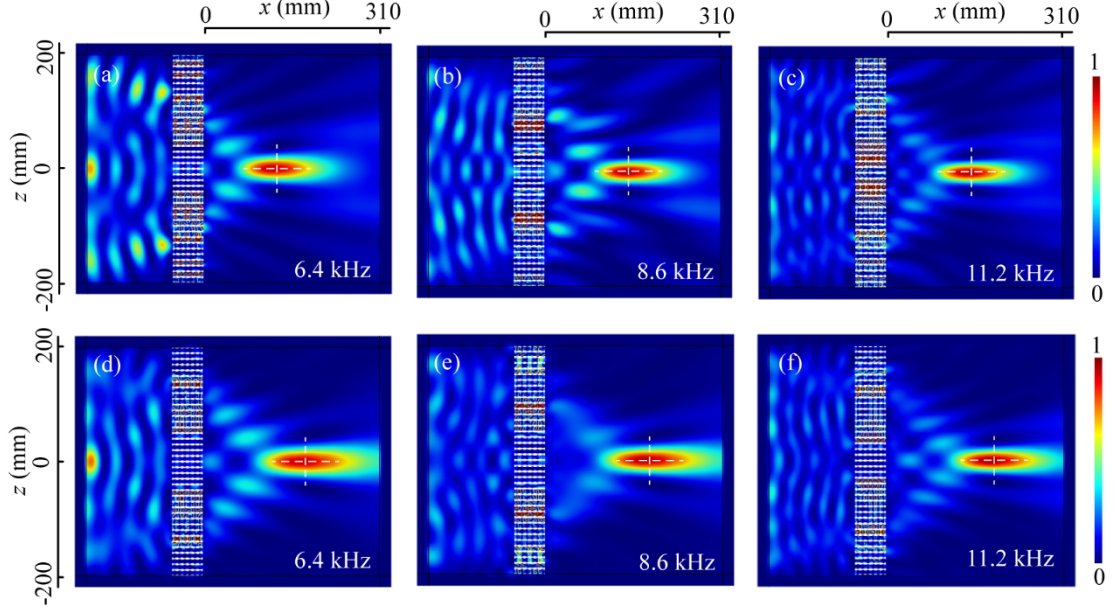


Fig. 6 The intensity of the out-of-plane wave fields with $f= 6.4, 8.6$ and 11.2 kHz. The focal positions are (a-c) $(150 \text{ mm}, 0)$ and (d-f) $(200 \text{ mm}, 0)$.

At last, we designed a structure with two metasurfaces to achieve asymmetric transmission of the flexural wave. As shown in Fig. 7, two elastic metasurfaces (EM1 and EM2) are set parallel with the distance of $d=250$ mm. The refraction angle of EM2 is designed as 90° in case of normal incidence. When the flexural wave is incident normally from the negative direction (ND), the propagating wave will be converted into an evanescent wave which cannot propagate through the structure. While when the wave comes from the positive direction (PD), the propagation direction can be tuned by EM1 to make sure that it can propagate through EM2.

First consider the wave coming from the ND. The phase shift of EM2, $\phi_2(z)$, can be easily determined by the GSL

$$\sin \theta_r - \sin \theta_i = 1 = \frac{\lambda_0}{2\pi} \frac{d\phi_2(z)}{dz} \quad (10)$$

with $\theta_i = 0^\circ$ and $\theta_r = 90^\circ$. Then consider the wave propagation along the PD. The phase shift of EM1, $\phi_1(z)$, can be expressed as

$$\sin \theta_{t1} - \sin \theta_i = \frac{\lambda_0}{2\pi} \frac{d\phi_1(z)}{dz}, \quad (11)$$

At the same time $\phi_2(z)$ should satisfy the following expression

$$\sin \theta_{t2} - \sin \theta_{t1} = \frac{\lambda_0}{2\pi} \frac{d\phi_2(z)}{dz}, \quad (12)$$

where θ_{t2} and θ_{t1} are the two propagating directions modulated by EM1 and EM2 as shown in Fig. 7(a). So for a given θ_{t2} ($|\sin \theta_{t2} - 1| \leq 1$), θ_{t1} can be obtained from Eqs. (10) and (12); and then substituting θ_{t1} into Eq. (11), we can get $\phi_1(z)$.

Taking $\theta_{t2} = 30^\circ$ as an example, Figs. 7(b)-(g) exhibit the results of numerical simulation for $f=6.4, 8.6$ and 11.2 kHz, respectively. When the flexural wave is incident from the PD, the transmitted wave propagates along the designated angle. When the

flexural wave is incident from the ND, it is converted into an evanescent wave by the EM2 and cannot propagate through the structure. It is noticed that the incident wave is not completely converted to the surface wave modes in Fig. 7(g). This can be interpreted by two reasons. The first one is that the incident wave beam is of finite width (as shown by the dotted lines in the figures), so scattering may appear at the edges of the beam. Secondly, as mentioned before, high-order diffractions may occur for large angle refraction [46, 47]. Even though, the asymmetric transmission can be well achieved by the proposed elastic metasurface in a wide frequency range. The screw-in depths of all units of EM1 and EM2 are listed in Table B3 in Appendix B.

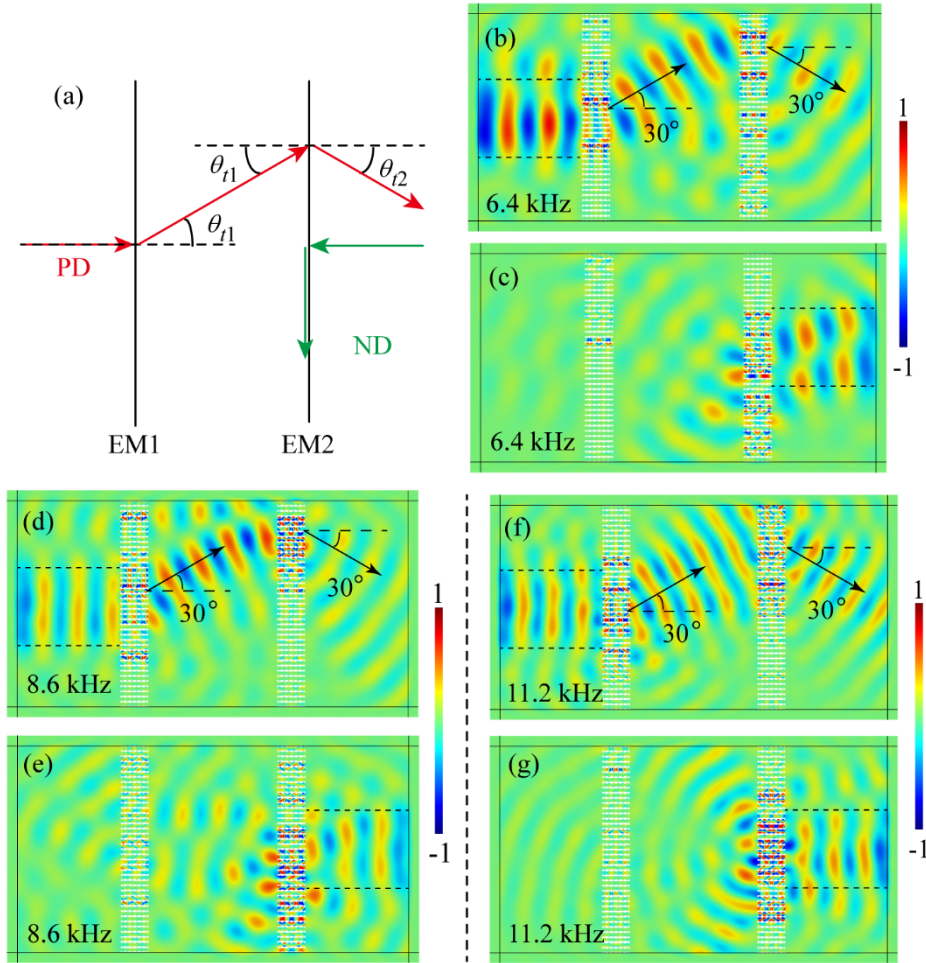


Fig. 7 (a) Schematic diagram of asymmetric transmission with red arrows representing PD and green arrows representing ND. The out-of-plane displacement fields of (b)-(c) 6.4 kHz, (d)-(e) 8.6 kHz and (f)-(g) 11.2 kHz. (b), (d), (f) are the results of PD, and (c), (e), (g) are those of ND.

The experimental demonstration

In this section, the functions of abnormal refraction and wave focusing are testified experimentally. The experiment platform with the manufactured plate (1650 mm×1100 mm×4 mm) is shown in Fig. 3(a). Figs. 3(e) and (f) show the zoomed-in diagrams of the metasurface. The signal generator (AFG 3102) generated a burst signal and the operation steps are similar as those of the functional element which are not stated here

for brevity. An array of 18 piezoelectric patches ($20\text{ mm}\times 20\text{ mm}\times 1\text{ mm}$) are bonded on the surface of the plate as excitations. In order to suppress the symmetrical wave mode, the out-of-plane excitation is applied only on one-side of the plate. As well known, the wave mode excited in this way is flexure-dominated. The out-of-plane displacements of scan areas 1 and 2 (corresponding to the same regions of Fig. 4(a)) are picked up. Blue-tacks are glued on the boundaries of the plate [13, 14], and the homogeneous regions are big enough; all these could well reduce the wave reflection.

For abnormal refraction, we consider the normal incident flexural wave of 6.4 kHz refracted along 15° . Figs. 8(a) and (c) are the simulated and experimental results, respectively. The polar directivity diagrams of Figs. 8(b) and (d) can be obtained from the out-of-plane displacement values of the vertical black lines in Figs. 8(a) and (c). It can be seen that the experimental results agree well with the simulation ones and the flexural waves propagate well along 15° . Due to the robustness of the structure, in a narrow frequency range of 6.3-6.5 kHz, 15° -refraction can still be achieved without changing the screw-in depth s , as shown in Figs. 8(e)-(l). But for other frequencies, s should be changed.

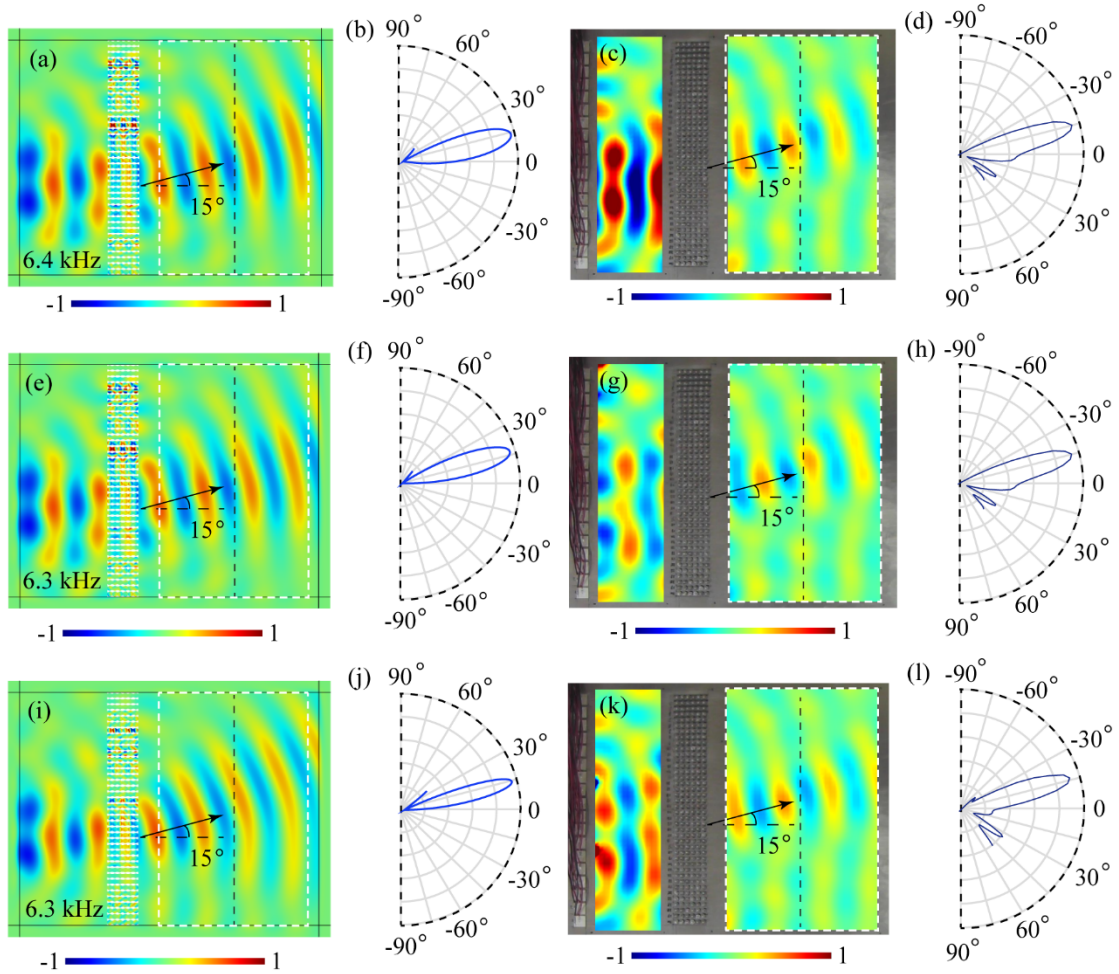


Fig. 8 The out-of-plane displacement fields of 15° refraction for 6.4 kHz obtained by (a) numerical simulation and (c) experiment; (b), (d) The polar directivity graphs correspond to the results of (a), (c), respectively. (e)-(h) and (i)-(l) are the results of 6.3 kHz and 6.5 kHz with the

same metasurface, respectively.

Now we demonstrate the wave focusing experimentally. Firstly, the focusing position of the flexural wave with $f = 6$ kHz is designed as $(x, z) = (150 \text{ mm}, 0)$ in the case of normal incidence. Figs. 9(a) and (d) are the out-of-plane displacement fields of simulation and experiment, respectively. Figs. 9(b) and (e) show the values along the transverse black dashed lines of Figs. 9(a) and (d), respectively. Figs. 9(c) and (f) are that of the vertical black dashed lines. The maximal values are marked by red asterisks. Next, the focusing position is still $(x, z) = (150 \text{ mm}, 0)$, but the frequency is changed to 6.4 kHz. The simulated and experimental results are shown in Fig. 10. Fig. 11 shows the results for $f = 6.4$ kHz and focusing position being $(x, z) = (200 \text{ mm}, 0)$. We can clearly see that the transmitted waves can be well focused on the expected positions, and the simulated results are well consistent with the experimental ones. All these validate the excellent focus performance of the metasurface.

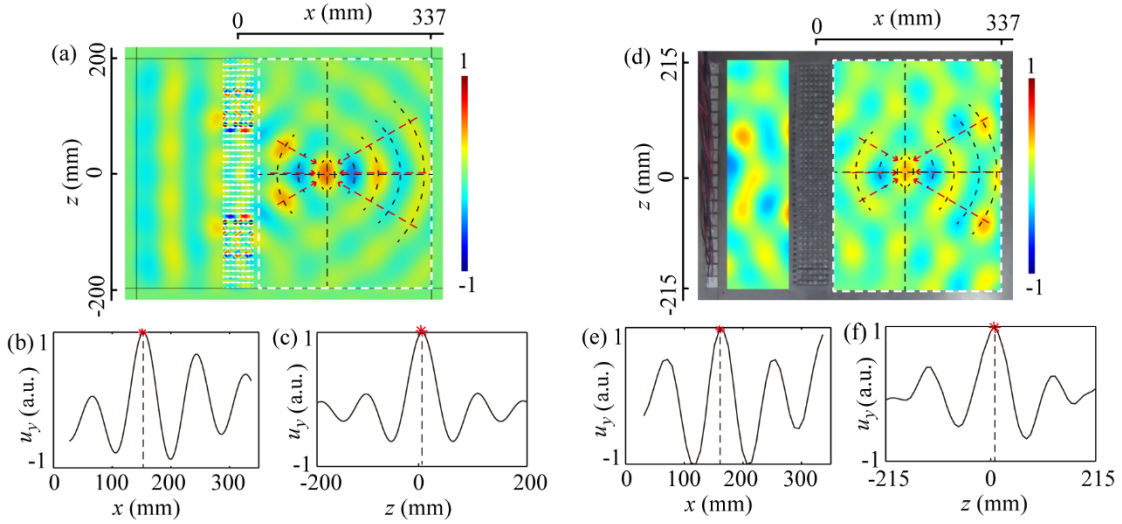


Fig. 9 The wave focusing results of $(x, z) = (150 \text{ mm}, 0)$ for $f = 6$ kHz. (a) The out-of-plane displacement fields of numerical simulation. The values along the transverse (b) and vertical (c) black dashed lines of Fig. 9(a). (d)-(f) are the experimental counterparts of (a)-(c).

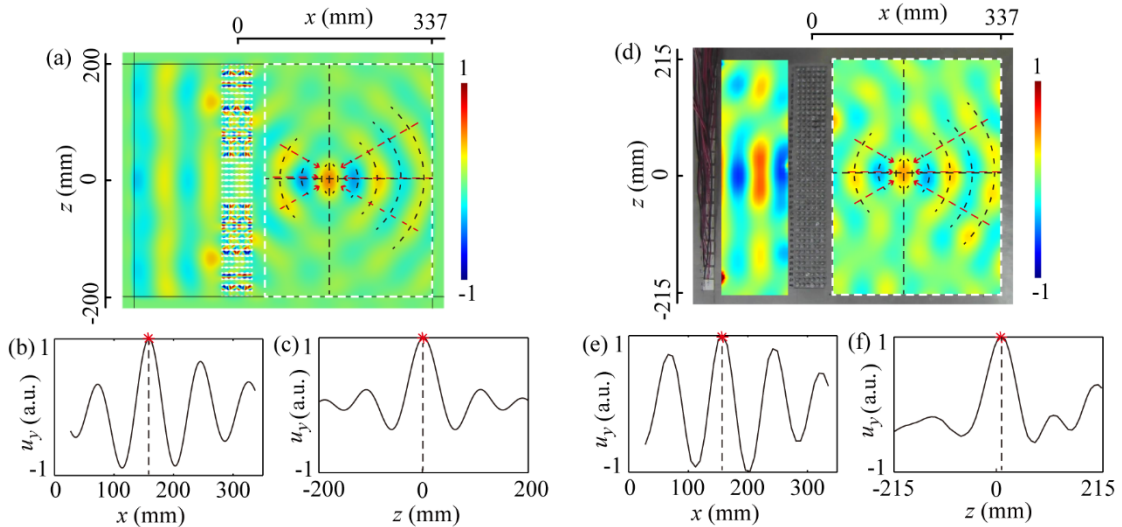


Fig. 10 The wave focusing results of $(x, z) = (150 \text{ mm}, 0)$ for $f = 6.4 \text{ kHz}$. (a) The out-of-plane displacement fields of numerical simulation. The values along the transverse (b) and vertical (c) black dashed lines of Fig. 10(a). (d)-(f) are the experimental counterparts of (a)-(c).

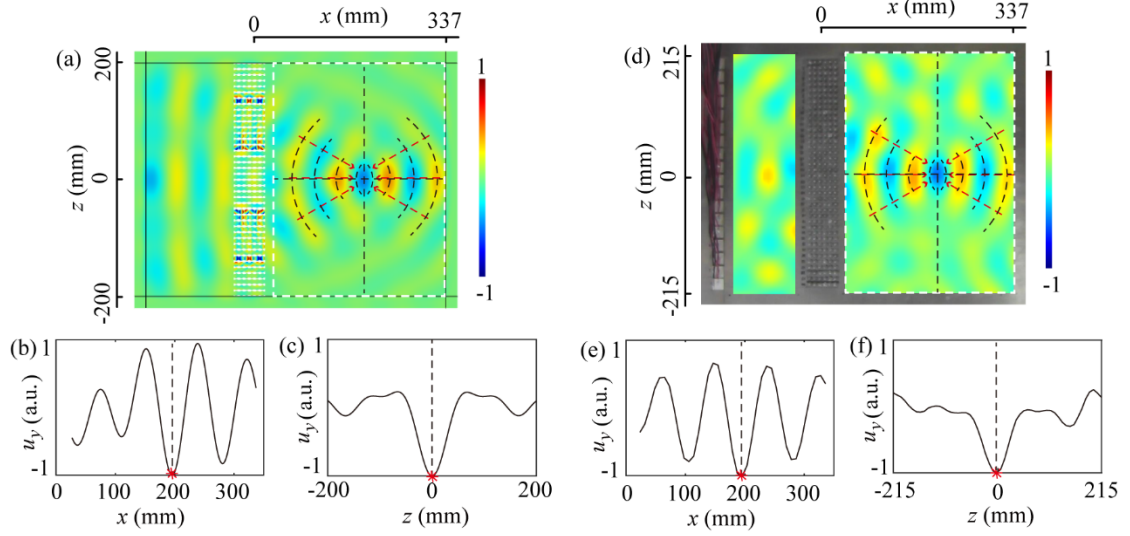


Fig. 11 The wave focusing results of $(x, z) = (200 \text{ mm}, 0)$ for $f = 6.4 \text{ kHz}$. (a) The normalized out-of-plane displacement fields of numerical simulation. The values along the transverse (b) and vertical (c) black dashed lines of Fig. 11(a). (d)-(f) are the experimental counterparts of (a)-(c).

Conclusion

In this research, a broadband reconfigurable metasurface has been conceived, designed and realized to control the wavefront of flexural waves based on the “screw-and-nut” operating mechanism. By changing the screw-in depths of the nuts, full 2π phase shift and high transmittance have been obtained over a large frequency range. Abnormal refraction and wave focusing functionalities have been demonstrated numerically and experimentally. In addition, a structure with two parallel metasurfaces is constructed to demonstrate the asymmetric transmission under different operating frequencies. The proposed broadband elastic metasurface with continuous tunability proposed in this work is of great significance, making an important progress to achieve pragmatic engineering applications on elastic wave manipulation. It should be noticed that the “broadband wave control” of this paper refers to the active control. It is necessary to change the screw-in depths of the nuts when switching between different functions and different frequencies.

Finally, we would like to mention that the present design of the metasurface is based on the GSL which cannot eliminate higher order diffractions in unwanted directions. In order to solve this problem, the lattice diffraction theory can be adopted in designing metasurfaces. However, it is a non-trivial task, especially for complex functionalities, such as wave focusing, beam bending, etc. Generally, an optimization method should be employed to completely suppress high-order diffractions [47]. This should be an interesting topic in a future work.

Acknowledgments

This project is supported by the National Natural Science Foundation of China (Grant Nos. 11872101, 11991031 and 12021002).

References

- [1] J. Park, D. Lee, J. Rho, Recent advances in non-traditional elastic wave manipulation by macroscopic artificial structures, *Appl. Sci.* 10 (2020), 547.
- [2] J. Hyun, M. Kim, W. Choi, Partitioned gradient-index phononic crystals for full phase control, *Sci. Rep.* 10 (2020), 14630.
- [3] C.L. Holloway, E.F. Kuester, J.A. Gordon, J. O'Hara, J. Booth, D.R. Smith, An overview of the theory and applications of metasurfaces: the two-dimensional equivalents of metamaterials, *IEEE Antennas Propag. Mag.* 54 (2012), 10-35.
- [4] H. Chen, A.J. Taylor, N.F. Yu, A review of metasurfaces: physics and applications, *Rep. Prog. Phys.* 79 (2016), 076401.
- [5] F. Ding, A. Pors, S. I. Bozhevolnyi, Gradient metasurfaces: a review of fundamentals and applications, *Rep. Prog. Phys.* 81 (2018), 026401.
- [6] P. Bharadwaj, B. Deutsch, L. Novotny, Optical antennas, *Adv. Opt. Photonics* 1 (2009), 438-483.
- [7] L. Novotny, N. van Hulst, Antennas for light, *Nat. Photonics* 5 (2011), 83-90.
- [8] B. Assouar, B. Liang, Y. Wu, Y. Li, J.C. Cheng, Y. Jing, Acoustic metasurfaces, *Nat. Rev. Mater.* 3 (2018), 460-472.
- [9] A.L. Chen, Q.Y. Tang, H.Y. Wang, S.D. Zhao, Y.S. Wang, Multifunction switching by a flat structurally tunable acoustic metasurface for transmitted waves, *Sci. China-Phys. Mech. Astron.* 63 (2020), 244611.
- [10] X.Y. Peng, J. F. Li, C. Shen, S. A. Cummer, Efficient scattering-free wavefront transformation with power flow conformal bianisotropic acoustic metasurfaces, *Appl. Phys. Lett.* 118 (2021), 061902.
- [11] C. Zhang, W.K. Cao, L.T. Wu, J.C. Ke, Y. Jing, T.J. Cui, Q. Cheng, A reconfigurable active acoustic metalens, *Appl. Phys. Lett.* 118 (2021), 133502.
- [12] H. Song, X.D. Ding, Z.X. Cui, H.H. Hu, Research progress and development trends of acoustic metamaterials, *Molecules* 26 (2021), 4018.
- [13] H.F. Zhu, F. Semperlotti, Anomalous refraction of acoustic guided waves in solids with geometrically tapered metasurfaces, *Phys. Rev. Lett.* 117 (2016), 034302.
- [14] L.Y. Cao, Z.C. Yang, Y.L. Xu, B. Assouar, Deflecting flexural wave with high transmission by using pillared elastic metasurface, *Smart Mater. Struct.* 27 (2018), 075051.
- [15] W. Wang, J. Iglesias, Y.b. Jin, B. Djafari-Rouhani, A. Khelif, Experimental realization of a pillared metasurface for flexural wave focusing, *APL Mater.* 9 (2021), 051125.
- [16] Y.B. Jin, B. Bonello, R.P. Moiseyenko, Y. Pennec, O. Boyko, B. Djafari-Rouhani, Pillar-type acoustic metasurface, *Phys. Rev. B* 96 (2017), 104311.
- [17] L.Y. Cao, Z.C. Yang, Y.L. Xu, Z.L. Chen, Y.F. Zhu, S.W. Fan, K. Donda, B. Vincent, B. Assouar, Pillared elastic metasurface with constructive interference for flexural wave manipulation, *Mech. Syst. Signal Pr.* 146 (2021), 107035.
- [18] Y.B. Jin, W. Wang, A. Khelif, B. Djafari-Rouhani, Elastic metasurfaces for deep and robust subwavelength focusing and imaging, *Phys. Rev. Appl.* 15 (2021), 024005.
- [19] W. Wang, J. Iglesias, Y.B. Jin, B. Djafari-Rouhani, A. Khelif, Experimental realization of a pillared metasurface for flexural wave focusing. *APL Mater.* 9 (2021), 051125.

- [20] L.Y. Cao, Z.C. Yang, Y.L. Xu, S.W. Fan, Y.F. Zhu, Z.L. Chen, B. Vincent, B. Assouar, Disordered elastic metasurfaces, *Phys. Rev. Applied* 13 (2020), 014054.
- [21] Y.Q. Liu, Z.X. Liang, F. Liu, O. Diba, A. Lamb, J. Li, Source illusion devices for flexural lamb waves using elastic metasurfaces, *Phys. Rev. Lett.* 119 (2017), 034301.
- [22] B. Li, Y.B. Hu, J.L. Chen, G.Y. Su, Y.Q. Liu, M.Y. Zhao, Z. Li, Efficient asymmetric transmission of elastic waves in thin plates with lossless metasurfaces, *Phys. Rev. Applied* 14 (2020), 054029.
- [23] G.Y. Su, Y.H. Zhang, Y.Q. Liu, Wang, T.J. Wang, Steering flexural waves by amplitude-shift elastic metasurfaces, *J. Appl. Mech.-Trans. ASME* 88 (2021), 051011.
- [24] Y.B. Hu, Y.H. Zhang, G.Y. Su, M.Y. Zhao, B. Li, Y.Q. Liu, Z. Li, Realization of ultrathin waveguides by elastic metagratings, *Commun. Phys.* 5 (2022), 62.
- [25] J. Zhang, X.B. Zhang, F.L. Xu, X.Y. Ding, M.X. Deng, N. Hu, C.Z. Zhang, Vibration control of flexural waves in thin plates by 3D-printed metasurfaces, *J. Sound Vib.* 481 (2020), 115440.
- [26] Z.B. Lin, W.K. Xu, C.M. Xuan, W.C. Qi, W. Wang, Modular elastic metasurfaces with mass oscillators for transmitted flexural wave manipulation, *J. Phys. D: Appl. Phys.* 54 (2021), 255303.
- [27] H. Lee, J.K. Lee, H.M. Seung, Y.Y. Kim, Mass-stiffness substructuring of an elastic metasurface for full transmission beam steering, *J. Mech. Phys. Solids* 112 (2018), 577-593.
- [28] S.W. Lee, H.M. Seung, W. Choi, M. Kim, J.H. Oh, Broad-angle refractive transmodal elastic metasurface, *Appl. Phys. Lett.* 117 (2020), 213502.
- [29] S.W. Lee, Y.J. Shin, H.W. Park, H.M. Seung, J.H. Oh, Full-wave tailoring between different elastic media: a double-unit elastic metasurface, *Phys. Rev. Appl.* 16 (2021), 064013.
- [30] J.J. Rong, W.J. Ye, S.Y. Zhang, Y.J. Liu, Frequency-coded passive multifunctional elastic metasurfaces, *Adv. Func. Mater.* 30 (2020), 2005285.
- [31] W.K. Xu, M. Zhang, Z.B. Lin, C.L. Liu, W.C. Qi, W. Wang, Anomalous refraction manipulation of Lamb waves using single-groove metasurfaces, *Phys. Scr.* 94 (2019), 105807.
- [32] Y.Q. Jiang, Y.L. Liu, M.Q. Kou, H.B. Li, X.P. Wu, X.J. Zeng, X.Y. Bi, H. Zhang, N. Hu, Multi-parameter independent manipulation for flexural wave by notched metasurface, *Int. J. Mech. Sci.* 214 (2022), 106928.
- [33] X.S. Su, A. N. Norris, Focusing, refraction, and asymmetric transmission of elastic waves in solid metamaterials with aligned parallel gaps, *J. Acoust. Soc. Am.* 139 (2016), 3386–3394.
- [34] H. Qiu, F.X. Li, Manipulation of shear horizontal guided wave with arbitrary wave fronts by using metasurfaces, *J. Phys. D: Appl. Phys.* 53 (2020), 285301.
- [35] L.H. Zeng, J. Zhang, Y.L. Liu, Y.X. Zhao, N. Hu, Asymmetric transmission of elastic shear vertical waves in solids, *Ultrasonics* 96 (2019), 34–39.
- [36] Y.C. Su, T.Y. Chen, L.H. Ko, M.H. Lu, Design of metasurfaces to enable shear horizontal wave trapping, *J. Appl. Phys.* 128 (2020), 175107.
- [37] Y.F. Wang, Y.Z. Wang, B. Wu, W.Q. Chen, Y.S. Wang, Tunable and active phononic crystals and metamaterials, *Appl. Mech. Rev.* 72 (2020), 040801.
- [38] J. Marconi, E. Riva, M.D. Ronco, G. Cazzulani, F. Braghin, M. Ruzzene, Experimental observation of nonreciprocal band gaps in a space-time-modulated beam using a shunted piezoelectric array, *Phys. Rev. Appl.* 13 (2020), 031001.
- [39] S.L. Li, J.W. Xu, J. Tang, Tunable modulation of refracted lamb wave front facilitated by adaptive elastic metasurfaces, *Appl. Phys. Lett.* 112 (2018), 021903.
- [40] R.Y. Xia, J.L. Yi, Z. Chen, Z. Li, In situ steering of shear horizontal waves in a plate by a tunable electromechanical resonant elastic metasurface, *J. Phys. D: Appl. Phys.* 53 (2019), 122040.

- [41] Y.Y. Chen, X.P. Li, H. Nassar, G.K. Hu, G.L. Huang, A programmable metasurface for real time control of broadband elastic rays, *Smart. Mater. Struct.* 27 (2018), 115011.
- [42] S.M. Yuan, A.L. Chen, Y.S. Wang, Switchable multifunctional fish-bone elastic metasurface for transmitted plate wave modulation, *J. Sound Vib.* 470 (2020), 115168.
- [43] S.M. Yuan, A.L. Chen, L.Y. Cao, H.W. Zhang, S.W. Fan, B. Assouar, Y.S. Wang, Tunable multifunctional fish-bone elastic metasurface for the wavefront manipulation of the transmitted in-plane waves, *J. Appl. Phys.* 128 (2020), 224502.
- [44] M.H. Bae, J.H. Oh, Nonlinear elastic metamaterial for tunable bandgap at quasi-static frequency, *Mech. Syst. Signal Pr.* 170 (2022), 108832.
- [45] N.F. Yu, P. Genevet, M.A. Kats, F. Aieta, J. Tetienne, F. Capasso, Z. Gaburro, Light propagation with phase discontinuities: generalized laws of reflection and refraction, *Science* 334 (2011), 333-337.
- [46] S. Larouche, D.R. Smith, Reconciliation of generalized refraction with diffraction theory, *Opt. Lett.* 37 (2012), 166419.
- [47] H.T. Zhou, W.X. Fu, Y.F. Wang, Y.S. Wang, High-efficiency Ultrathin Nonlocal Waterborne Acoustic Metasurface, *Phys. Rev. Appl.* 15 (2021), 044046.

Appendix A Effects of structure parameters in design of elastic metasurfaces

The influences of different structural parameters (n_1 , h_1 , h_5 , h_6 and h_7 , where n_1 is the number of basic units in a functional element) on the variation of phase shift and transmittance with the screw-in depth are discussed in this appendix. We first obtain the results for a set of parameters: $n_1 = 6$, $h_1 = 3$ mm, $h_5 = 2.5$ mm, $h_6 = 3$ mm and $h_7 = 8$ mm. Then we alter the value of n_1 (here we take $n_1 = 4, 5, 6$ and 7) with other parameters unchanged, calculate the curves, and illustrate them in Fig. A1. We can observe from the figure that with the increase of n_1 , the coverage interval of phase shift ϕ (black solid line) gradually increases and cover a full 2π range with high transmittance ξ_f (red dotted line) until $n_1 = 6$. In order to keep the thickness of metasurface as small as possible, we take $n_1 = 6$. Similarly, we change other parameters, h_1 , h_5 , h_6 or h_7 , one by one to discuss their influences on phase shift and transmittance. The results are presented in Figs. A2-A5. The shadowed areas represent the cases with low transmittance. It can be clearly seen that with the gradual increase of n_1 , h_1 , h_5 and h_7 , the resonance is gradually enhanced, and the phase shift can gradually cover a 2π range with high transmittance. With the increase of h_6 , the resonance becomes weaker and the coverage interval of phase shift decreases. In design of a metasurface, it should be ensured that the phase shift with high transmittance should cover a full 2π range.

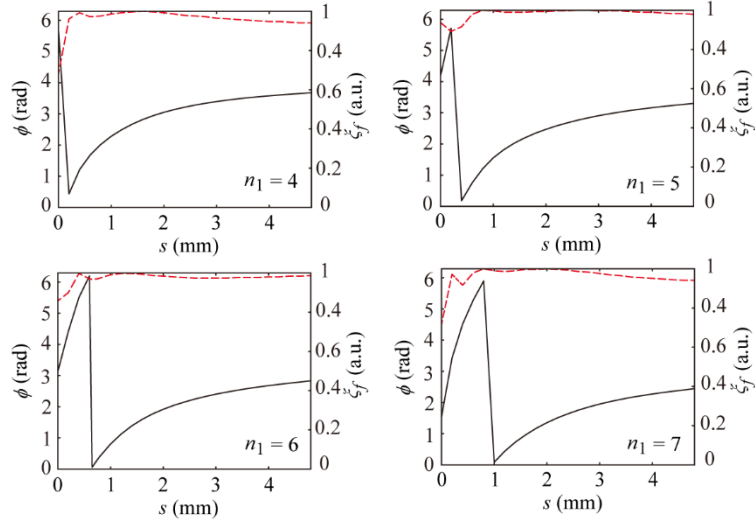


Fig. A1 Phase shift (black solid line) and transmittance (red dotted line) as functions of screw-in depth s for different n_1 at $f = 5.6$ kHz.

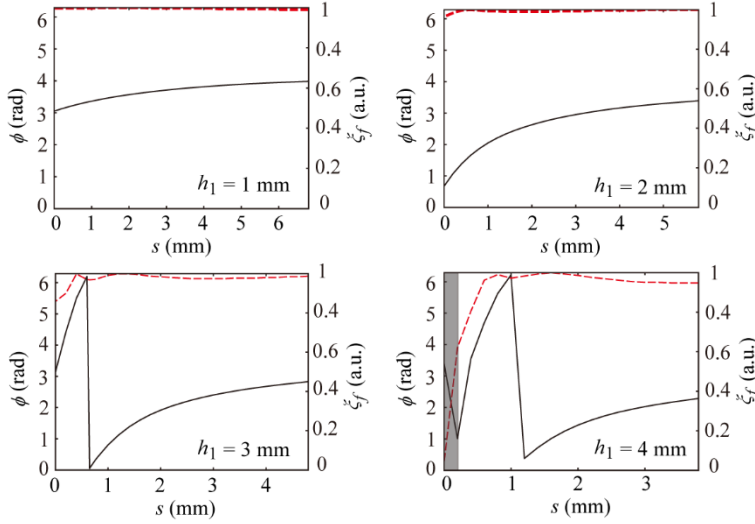


Fig. A2 Phase shift (black solid line) and transmittance (red dotted line) as functions of screw-in depth s for different h_1 at $f = 5.6$ kHz.

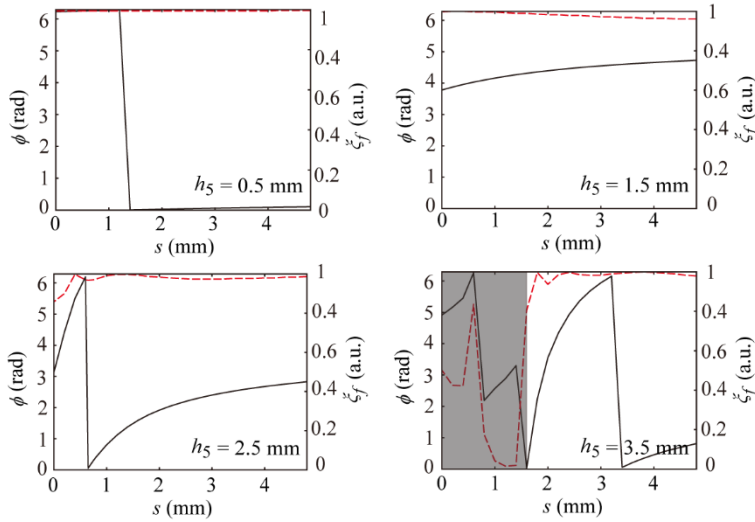


Fig. A3 Phase shift (black solid line) and transmittance (red dotted line) as functions of screw-in depth s for different h_5 at $f = 5.6$ kHz.

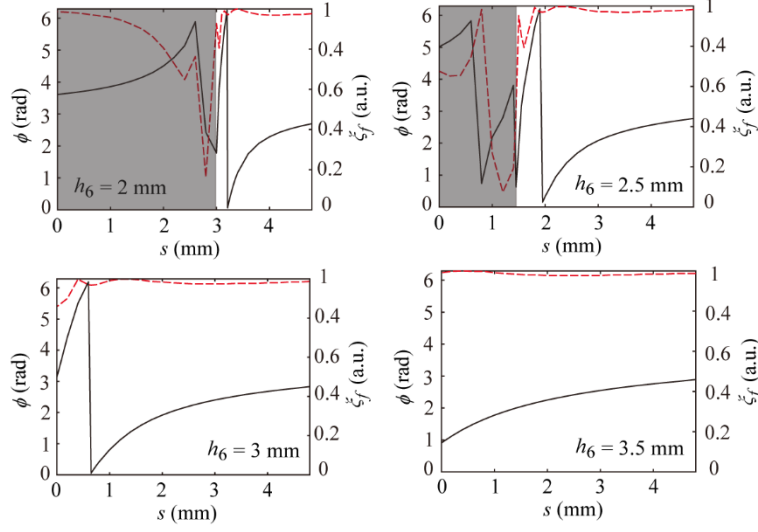


Fig. A4 Phase shift (black solid line) and transmittance (red dotted line) as functions of screw-in depth s for different h_6 at $f = 5.6$ kHz.

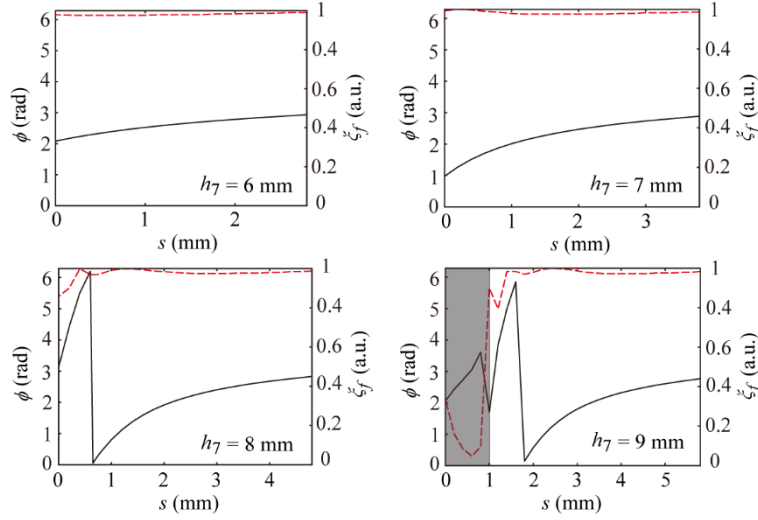


Fig. A5 Phase shift (black solid line) and transmittance (red dotted line) as functions of screw-in depth s for different h_7 at $f = 5.6$ kHz.

Appendix B The screw-in depths of the nuts

The following three tables show the screw-in depths of the nuts for various functions at different frequencies.

Table B1. The screw-in depths of the nuts in the n th functional element for the 15° and 50° directional refractions. (unit: mm).

s_i	15°			50°		
	6.4 kHz	8.6 kHz	11.2 kHz	6.4 kHz	8.6 kHz	11.2 kHz
s_1	3.39	3.89	3.49	3.39	3.89	3.49

s_2	3.98	4.18	3.50	0.79	2.33	3.53
s_3	4.81	4.55	3.51	0.85	2.40	3.57
s_4	0.79	2.33	3.53	0.93	2.46	3.64
s_5	0.80	2.35	3.54	1.04	2.54	3.73
s_6	0.83	2.38	3.56	1.16	2.66	3.85
s_7	0.85	2.40	3.57	1.31	2.83	4.04
s_8	0.88	2.42	3.59	1.52	3.06	4.34
s_9	0.90	2.44	3.61	1.84	3.42	4.80
s_{10}	0.94	2.46	3.64	2.31	4.08	3.54
s_{11}	0.97	2.49	3.67	3.16	2.35	3.59
s_{12}	1.01	2.51	3.70	0.78	2.41	3.67
s_{13}	1.05	2.55	3.74	0.84	2.48	3.76
s_{14}	1.09	2.58	3.77	0.91	2.57	3.90
s_{15}	1.13	2.62	3.81	1.02	2.70	4.12
s_{16}	1.17	2.67	3.86	1.14	2.88	4.47
s_{17}	1.22	2.73	3.91	1.28	3.12	3.51
s_{18}	1.27	2.79	3.98	1.48	3.54	3.55
s_{19}	1.32	2.85	4.06	1.77	4.30	3.60
s_{20}	1.39	2.92	4.15	2.21	2.36	3.70
s_{21}	1.47	2.99	4.25	2.97	2.43	3.80
s_{22}	1.55	3.08	4.37	4.78	2.49	3.96
s_{23}	1.65	3.19	4.52	0.83	2.59	4.21
s_{24}	1.75	3.32	4.71	0.90	2.74	4.62
s_{25}	1.88	3.47	3.50	1.00	2.92	3.52
s_{26}	2.02	3.67	3.51	1.12	3.20	3.57
s_{27}	2.19	3.90	3.53	1.26	3.67	3.63
s_{28}	2.39	4.19	3.55	1.44	4.56	3.73
s_{29}	2.63	2.31	3.56	1.72	2.38	3.84
s_{30}	2.94	2.33	3.58	2.13	2.44	4.03
s_{31}	3.34	2.36	3.59	2.81	2.51	4.31
s_{32}	3.98	2.38	3.62	4.34	2.62	4.80
s_{33}	4.81	2.40	3.65	0.81	2.78	3.54
s_{34}	0.79	2.42	3.68	0.89	2.98	3.58
s_{35}	0.80	2.44	3.71	0.99	3.29	3.66
s_{36}	0.83	2.46	3.75	1.10	3.83	3.76
s_{37}	0.85	2.49	3.78	1.23	4.80	3.89
s_{38}	0.88	2.51	3.82	1.41	2.39	4.10
s_{39}	0.90	2.55	3.87	1.67	2.46	4.44
s_{40}	0.94	2.58	3.93	2.05	2.53	3.50

Table B2. The screw-in depths of the nuts in the n th functional element for the wave focusing.
(unit: mm).

s_i	(150 mm, 0)				(200 mm, 0)		
	6 kHz	6.4 kHz	8.6 kHz	11.2 kHz	6.4 kHz	8.6 kHz	11.2 kHz

s_1	3.30	0.88	2.52	3.83	3.69	2.37	3.61
s_2	2.18	0.80	2.44	3.72	2.62	2.31	3.56
s_3	1.63	3.98	2.38	3.62	2.09	3.76	3.52
s_4	1.28	2.68	4.65	3.57	1.74	3.31	4.69
s_5	1.04	2.08	3.75	3.52	1.50	3.04	4.31
s_6	0.87	1.72	3.27	4.64	1.33	2.86	4.07
s_7	0.75	1.47	2.99	4.25	1.21	2.72	3.91
s_8	0.66	1.29	2.82	4.02	1.12	2.62	3.80
s_9	0.57	1.17	2.68	3.86	1.04	2.54	3.73
s_{10}	0.50	1.08	2.57	3.77	0.97	2.49	3.67
s_{11}	0.46	1.00	2.50	3.69	0.91	2.45	3.62
s_{12}	0.42	0.92	2.46	3.63	0.87	2.41	3.58
s_{13}	3.83	0.87	2.42	3.59	0.83	2.38	3.56
s_{14}	2.90	0.83	2.38	3.56	0.80	2.35	3.54
s_{15}	2.39	0.80	2.35	3.54	0.79	2.33	3.52
s_{16}	2.07	0.78	4.79	3.52	4.75	4.52	3.51
s_{17}	1.87	4.41	4.37	3.50	4.10	4.24	3.50
s_{18}	1.74	3.84	4.11	3.50	3.72	4.05	4.78
s_{19}	1.67	3.53	3.97	3.49	3.49	3.95	4.70
s_{20}	1.63	3.40	3.90	3.49	3.40	3.90	4.66
s_{21}	1.63	3.40	3.90	3.49	3.40	3.90	4.66
s_{22}	1.67	3.53	3.97	3.49	3.49	3.95	4.70
s_{23}	1.74	3.84	4.11	3.50	3.72	4.05	4.78
s_{24}	1.87	4.41	4.37	3.50	4.10	4.24	3.50
s_{25}	2.07	0.78	4.79	3.52	4.75	4.52	3.51
s_{26}	2.39	0.80	2.35	3.54	0.79	2.33	3.52
s_{27}	2.90	0.83	2.38	3.56	0.80	2.35	3.54
s_{28}	3.83	0.87	2.42	3.59	0.83	2.38	3.56
s_{29}	0.42	0.92	2.46	3.63	0.87	2.41	3.58
s_{30}	0.46	1.00	2.50	3.69	0.91	2.45	3.62
s_{31}	0.50	1.08	2.57	3.77	0.97	2.49	3.67
s_{32}	0.57	1.17	2.68	3.86	1.04	2.54	3.73
s_{33}	0.66	1.29	2.82	4.02	1.12	2.62	3.80
s_{34}	0.75	1.47	2.99	4.25	1.21	2.72	3.91
s_{35}	0.87	1.72	3.27	4.64	1.33	2.86	4.07
s_{36}	1.04	2.08	3.75	3.52	1.50	3.04	4.31
s_{37}	1.28	2.68	4.65	3.57	1.74	3.31	4.69
s_{38}	1.63	3.98	2.38	3.62	2.09	3.76	3.52
s_{39}	2.18	0.80	2.44	3.72	2.62	2.31	3.56
s_{40}	3.30	0.88	2.52	3.83	3.69	2.37	3.61

Table B3. The screw-in depths of the nuts in the n th functional element for the asymmetric transmission. (unit: mm).

s_i	6.4 kHz	8.6 kHz	11.2 kHz
-------	---------	---------	----------

	EM1 (30°)	EM2 (90°)	EM1 (30°)	EM2 (90°)	EM1 (30°)	EM2 (90°)
s_1	3.39	3.39	3.89	3.89	4.66	4.66
s_2	2.67	0.80	3.48	2.35	4.35	3.54
s_3	2.23	0.89	3.20	2.44	4.13	3.60
s_4	1.92	1.03	3.01	2.53	3.98	3.72
s_5	1.68	1.19	2.86	2.70	3.86	3.88
s_6	1.50	1.41	2.75	2.94	3.78	4.18
s_7	1.36	1.77	2.64	3.35	3.71	3.49
s_8	1.25	2.40	2.56	4.21	3.65	3.55
s_9	1.16	3.85	2.50	2.38	3.59	3.62
s_{10}	1.08	0.82	2.45	2.46	3.56	3.74
s_{11}	1.00	0.92	2.41	2.57	3.53	3.91
s_{12}	0.93	1.06	2.37	2.76	3.50	4.22
s_{13}	0.87	1.23	2.33	3.03	4.58	4.84
s_{14}	0.83	1.48	4.13	3.52	4.29	3.55
s_{15}	0.79	1.88	3.64	4.62	4.09	3.63
s_{16}	4.06	2.59	3.31	2.40	3.95	3.75
s_{17}	3.04	4.48	3.08	2.48	3.84	3.94
s_{18}	2.46	0.84	2.92	2.61	3.76	4.27
s_{19}	2.09	0.95	2.79	2.82	3.70	3.50
s_{20}	1.81	1.10	2.68	3.13	3.64	3.56
s_{21}	1.60	1.27	2.59	3.74	3.59	3.64
s_{22}	1.44	1.55	2.52	2.34	3.56	3.77
s_{23}	1.30	1.99	2.47	2.42	3.53	3.97
s_{24}	1.20	2.83	2.43	2.51	3.50	4.32
s_{25}	1.12	0.78	2.39	2.67	4.50	3.51
s_{26}	1.04	0.86	2.35	2.89	4.25	3.57
s_{27}	0.97	0.98	2.30	3.26	4.06	3.66
s_{28}	0.90	1.13	3.83	4.02	3.92	3.78
s_{29}	0.85	1.32	3.44	2.36	3.82	3.99
s_{30}	0.81	1.62	3.17	2.45	3.75	4.38
s_{31}	0.78	2.12	2.99	2.55	3.68	3.51
s_{32}	3.54	3.12	2.85	2.72	3.62	3.57
s_{33}	2.76	0.79	2.73	2.98	3.58	3.67
s_{34}	2.29	0.88	2.63	3.42	3.55	3.80
s_{35}	1.96	1.01	2.55	2.30	3.52	4.03
s_{36}	1.72	1.17	2.49	2.39	3.50	4.44
s_{37}	1.53	1.37	2.45	2.47	4.44	3.52
s_{38}	1.38	1.71	2.41	2.59	4.20	3.58
s_{39}	1.26	2.27	2.37	2.79	4.02	3.68
s_{40}	1.17	3.49	2.32	3.07	3.89	3.82